

Article

A Stable and Reusable Supported Copper Catalyst for the Selective Liquid-Phase Hydrogenation of 5-Hydroxymethylfurfural to 2,5-Bis(hydroxymethyl)furan

Juan Zelin, Camilo Ignacio Meyer, Hernán Antonio Duarte and Alberto Marchi *

Catalysis Science and Engineering Research Group (GICIC), Instituto de Investigaciones en Catálisis y Petroquímica (INCAPE), Universidad Nacional del Litoral (UNL)-Consejo Nacional de Investigaciones Científicas y Técnicas (CONICET), Colectora Ruta Nac. No. 168 Km 0, Santa Fe 3000, Argentina

* Correspondence: amarchi@fiq.unl.edu.ar; Tel.: +54-(0342)-451-1370/1546

Abstract: Synthesis of 2,5-bis(hydroxymethyl)furan (BHMF) by selective 5-hydroxymethylfurfural (HMF) hydrogenation is ecofriendly and industrially important since HMF is obtained from renewable sources, and BHMF is a raw material used for production of biodegradable polymers. Four copper-based catalysts were prepared by incipient wetness impregnation (Cu/SiO₂-I, Cu/Al₂O₃-I), precipitation–deposition (Cu/SiO₂-PD) and coprecipitation (CuMgAl), and then tested in the liquid-phase hydrogenation of HMF. Metallic phases with large copper particles were obtained by incipient wetness impregnation, while precipitation methods gave highly dispersed metal copper nanoparticles. The pattern found for the concentration and strength of surface acid sites was: CuMgAl > Cu/Al₂O₃-I > Cu/SiO₂-PD > Cu/SiO₂-I. The copper-based catalysts active in HMF hydrogenation are all highly selective to BHMF, but the intrinsic activity and stability depend on metallic copper dispersion and support nature. The catalyst stability becomes poorer in the cases that the metallic phase is formed by large copper particles or interacts with high-acidity supports. Therefore, the catalyst with the highest activity, BHMF yield and stability was Cu/SiO₂-PD. Furthermore, it was found that Cu/SiO₂-PD is reusable in the selective liquid-phase HMF hydrogenation after being submitted to a two-step thermal treatment: (1) calcination under air flow at 673 K; (2) reduction under H₂ flow at 523 K.

Keywords: copper-based catalysts; 5-hydroxymethylfurfural; 2,5-bis(hydroxymethyl)furan; furanic compounds; selective hydrogenation



Citation: Zelin, J.; Meyer, C.I.; Duarte, H.A.; Marchi, A. A Stable and Reusable Supported Copper Catalyst for the Selective Liquid-Phase Hydrogenation of 5-Hydroxymethylfurfural to 2,5-Bis(hydroxymethyl)furan.

Catalysts **2022**, *12*, 1476. <https://doi.org/10.3390/catal12111476>

Academic Editors: Monica Nardi, Svilen P. Simeonov and Herrera Cano
Natividad Carolina

Received: 5 October 2022

Accepted: 16 November 2022

Published: 19 November 2022

Publisher's Note: MDPI stays neutral with regard to jurisdictional claims in published maps and institutional affiliations.



Copyright: © 2022 by the authors. Licensee MDPI, Basel, Switzerland. This article is an open access article distributed under the terms and conditions of the Creative Commons Attribution (CC BY) license (<https://creativecommons.org/licenses/by/4.0/>).

1. Introduction

Biomass is a renewable source for chemical compounds that can replace those currently obtained from non-renewable fossil resources (oil, gas and coal). In this sense, the use of biomass as a source of raw materials for the industry could have a highly positive environmental impact [1–5]. As a consequence, there is growing technological attention on biomass to obtain chemical compounds of industrial interest, such as carbohydrates, which constitute two-thirds of the biomass around the world. In particular, the six-carbon-atom carbohydrates (hexoses), such as glucose and fructose, are the most abundant monosaccharides in nature and can be transformed into platform chemicals. Among these compounds, 5-hydroxymethylfurfural (HMF) might be considered, which is produced via dehydration of hexoses. HMF is known as a “sleeping giant” because of its high potential to bridge the gap between fossil-based and more sustainable chemistry. However, efficient HMF-based chemistry can still not be developed because its separation and purification from reaction media are very difficult. Furthermore, the HMF is highly reactive and easily degrades through hydrolysis and humification reactions [6]. These hurdles restrain the industrial production of the compounds derived from HMF. Awakening of HMF depends on the approach used to create a sustainable future [7]. The diversity of functional groups in

the HMF molecule gives a great number of possibilities for its application as a platform chemical for the production of biofuel, advanced materials, and several valuable chemicals [8–14]. A molecule that can be produced from HMF is 2,5-bis(hydroxymethyl)furan (BHMF), which is also considered among the twelve “sleeping giants”. This compound is already used as raw material to obtain biodegradable polymers, e.g., for the manufacture of polyurethane foam [15,16], and it is a promising diol for the synthesis of polyesters with a wide field of possible industrial applications [17]. In particular, polymers formed by condensation of BHMF with succinic acid, and subsequent cross-linking with bismaleimide, are materials with interesting self-healing properties [18,19].

BHMF can be obtained by selective hydrogenation of the C=O group of the HMF molecule (Figure 1), but HMF can also undergo hydrogenation of the aromatic ring or hydrogenolysis of the C-OH bonds to produce 2,5-bis(hydroxymethyl)tetrahydrofuran (BHMTF) or 2,5-dimethylfuran (DMF), respectively [17,20,21]. Among the most used catalysts in HMF hydrogenation are those based on supported noble metals, for example, Ru, Pd and Pt. Nevertheless, in addition to their high cost, the noble metal catalysts may give low selectivity to BHMF because 2,5-bis(hydroxymethyl) tetrahydrofuran (BHMTF) and 2,5-dimethylfuran (DMF) may be produced, and some linear polyols, e.g., 1,2,6-hexanetriol, 1,2,5,6-hexanetetrol and 1,2,5-hexanetriol, can also be formed through ring-opening reactions [17,20–23]. However, in some cases, high selectivity and yield to BHMF were obtained with noble-metal-based catalysts in the liquid-phase HMF hydrogenation under controlled reaction conditions. For example, at 323–373 K and 10–30 bar, with a commercial Ru (5 wt%)/C catalyst and water or ethanol as solvents, yields in BHMF between 80 and 93% were reached [24–26]. Several non-noble metal catalysts were tested in HMF hydrogenation as well. Despite this, generally, higher temperatures and pressures are necessary with non-noble versus with noble metal catalysts. The lower cost of non-noble metals makes them attractive to be used in liquid-phase hydrogenation reactions. High selectivity to BHMF was obtained with non-noble metal catalysts, such as Ni-Raney and Ni-supported catalysts, but BHMTF and DMF were also produced in important amounts with this type of Ni-based catalysts [27–29]. Instead, Cu-based catalysts were reported to be more selective to BHMF than Ni-based ones. For instance, Zu et al. used Cu/ZnO, with different Cu loading (40–80 wt%), and reported 99% HMF conversion with a 98% selectivity to BHMF after 5 h reaction at 373 K and 15 bar [30]. Under similar reaction conditions with Cu (50 wt%)/SiO₂, Upare et al. reached around 95% HMF conversion with 97% selectivity to BHMF after 4 h reaction time [31]. Recently, Hu et al. used Cu/Al₂O₃ with a relative low Cu content (5 wt%) obtaining HMF conversion levels of only 60% with a selectivity to BHMF of 92% at 393 K and 20 bar in a fixed bed reactor. However, HMF conversion and selectivity higher than 90% were achieved when potassium was employed as a promoter for the Cu (5wt%)/Al₂O₃ catalyst [32]. Cu/MgAlO_x catalysts were also employed in the hydrogenation of HMF reaching 97% conversion and a BHMF selectivity of 95% at 453 K and 10 bar. Unfortunately, these catalysts exhibit strong deactivation due to the strong adsorption of reactant and product molecules [33].

In summary, in previous works, several characterization studies and catalytic activity tests have been carried out for the liquid-phase hydrogenation of HMF using Cu catalysts with good activity and selectivity to BHMF. Nevertheless, there is a lack of studies on the possible causes of deactivation observed in some cases and on the feasibility of reusing these Cu-based catalysts. In this work, four Cu-based catalysts, prepared by different methods over distinct supports, were tested in the liquid-phase hydrogenation of HMF. The objective is to determine the influence of the physicochemical and structural properties of the Cu-based catalysts on their activity and stability for the selective hydrogenation of HMF to BHMF in the liquid phase. Finally, with the catalyst that showed the best performance, additional characterizations and post-reaction tests were carried out in order to ascertain the stability and reuse feasibility of this catalyst.

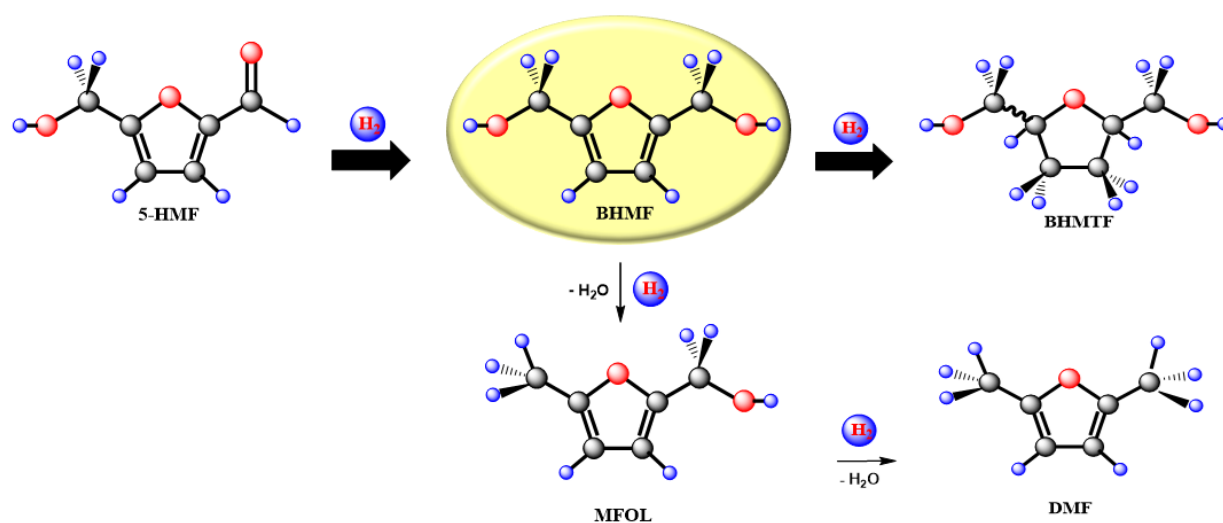


Figure 1. Reaction scheme for the hydrogenation of 5-hydroxymethylfurfural (HMF). Products: 2,5-bis(hydroxymethyl)furan (BHMf); 5-methyl-2-furanmethanol (MFOL); 2,5-dimethylfuran (DMF); 2,5-bis(hydroxymethyl)tetrahydrofuran (BHMtF).

2. Results and Discussions

2.1. Physicochemical Characterization

The results obtained from the physicochemical characterization of the copper-based catalysts used in this work are summarized in Table 1. The Cu loads, determined by AAS, were between 7 and 10 wt% in all of the cases.

Table 1. Physicochemical characterization of the Cu-based catalysts and supports.

Sample	Cu ^a (%w/t)	S _g (m ² g ⁻¹)	V _p (cm ³ g ⁻¹)	d _p (nm)	L _{CuO} ^b (nm)	L _{Cu} ^b (nm)	D _{Cu} ^c (%)	d _{Cu} ^d (nm)	TPR ^e T _M (K)	NH ₃ TPD ^f (μmol g ⁻¹)
SiO ₂	-	296	1.06	14.3	-	-	-	-	-	6.5
Al ₂ O ₃	-	190	0.47	9.96	-	-	-	-	-	61
Cu/SiO ₂ -I	7.7	260	0.93	13.0	26	39	2.0	38	614	23
Cu/SiO ₂ -PD	8.0	270	0.94	12.7	n.d.	n.d.	21	3.6	566	68
Cu/Al ₂ O ₃ -I	10.0	175	0.46	8.85	34	47	1.7	48	512–580	81
CuMgAl	7.1	291	0.63	12.6	n.d.	n.d.	11	-	518	230

^a Cu content determined by atomic absorption spectroscopy. ^b Mean crystallite size estimated by Scherrer's equation. ^c Metallic Cu dispersion determined by titration with N₂O at 363 K. ^d Cu metal particle size estimated from the metallic dispersion assuming cubic geometry. ^e Temperature at the maximum H₂ consumptions in TPR experiments. ^f Total acid site concentration determined by desorbed NH₃ in TPD measurements.

The specific surface areas (S_g) of Cu/SiO₂-I, Cu/SiO₂-PD and Cu/Al₂O₃-I calcined samples were 9 to 12% lower than those of the corresponding calcined supports, i.e., SiO₂ (296 m²g⁻¹) and γ-Al₂O₃ (190 m²g⁻¹). Pore volume (V_p) and pore mean diameter (d_p) showed a similar drop, i.e., between 10 and 12% with respect to the support. Thus, it can be asserted that the addition of Cu by the impregnation or precipitation–deposition methods did not significantly modify the textural properties of the support. On the other hand, CuMgAl mixed oxide prepared by co-precipitation at controlled pH, after subsequent calcination in air flow, showed a specific surface area of 291 m²g⁻¹, a pore volume of 0.63 cm³g⁻¹ and a pore mean diameter of 12.6 nm (Table 1). That is, a mixed oxide precursor with similar textural properties to the samples of supported catalyst precursors on SiO₂ and Al₂O₃ was obtained by the coprecipitation method. In summary, all of the catalyst precursors used in this work have similar textural properties and relatively high surface area and pore volume.

The X-ray powder diffractograms for both the calcined and reduced–passivated samples are shown in Figure 2A,B, respectively. For the Cu/SiO₂-I calcined sample (Figure 2A, Diffractogram (1)), all the diffraction peaks detected at 2θ > 30° can be assigned to a CuO polycrystalline phase with a tenorite-like structure (PDF 47–254). Considering the (002)

plane family and applying the Scherrer's equation, a mean crystallite size of about 26 nm was estimated (Table 1). The reduced-passivated Cu/SiO₂-I sample showed diffraction peaks at 43.3°, 50.3° and 74.1° (Figure 2B, diffractogram (1)), which correspond to (111), (200), (220) crystal planes of metallic Cu with *fcc* crystalline structure (PDF-2-4-0836). The estimated mean size of metallic Cu crystallites, considering the (111) plane family, was 39 nm (Table 1), 50% larger than the crystallite size of CuO on the calcined sample. For both the calcined and reduced-passivated samples of Cu/SiO₂-PD, only the amorphous halo at $2\theta < 30^\circ$, attributed to the SiO₂ support, was observed (Figure 2A,B, Diffractograms (3)). Diffraction peaks from CuO or metallic Cu were not observed, probably because the corresponding crystallites are very small and/or their crystalline structure is highly disordered. These crystallites may be less than 4 nm in size, which is the accepted detection limit for XRD. Instead, a polycrystalline phase of CuO was detected in the case of the calcined sample Cu/Al₂O₃-I, and diffraction peaks at 43.3°, 50.3° and 74° were observed in the reduced-passivated sample, which corresponds to a polycrystalline metallic Cu phase, (Figure 2A,B, Diffractograms (2)). The estimated average size of CuO and metallic Cu crystallites, considering the (002) and (111) crystal planes, were around 34 and 47 nm, respectively (Table 1), i.e., the crystallites are about 40% larger in average after reduction. The low intensity diffraction peaks at 37°, 45.7° and 66.7° can be assigned to the alumina support with a spinel-like structure (Al₂O₃ PDF 29-0063). In the case of the CuMgAl sample (Figure 2A,B, Diffractogram (4)), only diffraction peaks corresponding to a polycrystalline phase with a spinel-like structure were detected (MgAl₂O₄ PDF 48-1548). In CuMgAl mixed oxide, the Cu²⁺ ions are highly interdispersed in the spinel-like matrix of a non-stoichiometric magnesium aluminate, i.e., no CuO segregation occurs [34–36]. This explains the absence of CuO diffraction peaks in the X-ray diffractogram of CuMgAl (Figure 2A, Diffractogram (4)). The reduction of these Cu²⁺ ions, strongly interacting with the spinel-like matrix, gives as a result, a metallic Cu phase constituted by small crystallites, less than 4 nm in size, which explains the absence of metal Cu diffraction peaks in the X-ray diffractogram of reduced CuMgAl (Figure 2B, Diffractogram (4)).

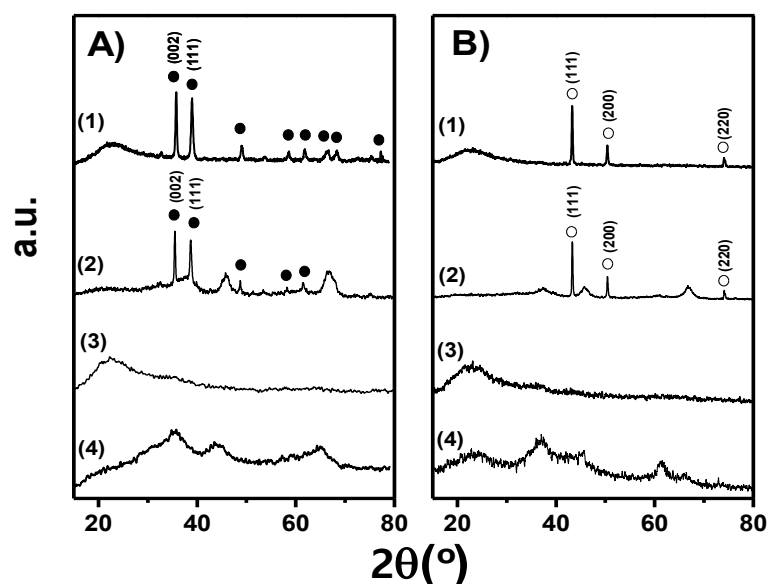


Figure 2. X-ray diffractograms of samples prepared in this work: (A) calcined oxide precursors and (B) reduced-passivated samples. (1) Cu/SiO₂-I, (2) Cu/Al₂O₃-I, (3) Cu/SiO₂-PD, (4) CuMgAl. ● CuO, ○ Cu.

The metallic Cu dispersion (D_{Cu}) was determined by N₂O decomposition after reduction of samples under H₂ flow (Table 1). The highest metallic Cu dispersion (21%), for the catalyst series used in this work, was reached with Cu/SiO₂-PD, which is twice higher than that of CuMgAl (11%). For samples prepared by the impregnation method,

Cu/Al₂O₃-I and Cu/SiO₂-I, the metallic dispersion was only 1.7% and 2.0%, respectively. Therefore, the metallic copper dispersion pattern was the following: Cu/SiO₂-PD > CuMgAl >> Cu/SiO₂-I \cong Cu/Al₂O₃-I. Furthermore, the metallic dispersion of Cu/SiO₂-PD was one order of magnitude higher than that one of Cu/SiO₂-I and Cu/Al₂O₃-I. Assuming cubic particles with a surface density of Cu atoms of 1.08×10^{-15} at/cm⁻², the mean sizes of metallic copper particles were estimated (Table 1). Thus, the size of metallic Cu particles determined for Cu/SiO₂-PD was around 3.6 nm, i.e., one order smaller than those estimated by Scherrer's equation for the metallic crystallite sizes of Cu/SiO₂-I and Cu/Al₂O₃-I, which is in agreement with the XRD results. In a previous work, we determined by TEM that the metallic Cu phase of a reduced-passivated Cu/SiO₂-PD sample, prepared by precipitation–deposition method under similar conditions, was mainly formed by metallic nanoparticles in the range of 3–4 nm, which were evenly dispersed on the support surface [34]. These particle sizes estimated by TEM measurements are in good agreement with the mean particle size obtained by titration with N₂O (Table 1). This result also accounts for the XRD ones, since no diffraction peaks due to crystallite metallic Cu could be detected in Cu/SiO₂-PD (Figure 2, Diffractogram (3)). On the other hand, for the samples prepared by incipient wetness impregnation, Cu/SiO₂-I and Cu/Al₂O₃-I, the metallic particle sizes determined by N₂O titration are 38 and 49 nm, respectively, i.e., ten times larger than those for Cu/SiO₂-PD. These mean particle sizes are close to the mean crystallite sizes estimated by Scherrer's equation (Table 1), suggesting that most copper particles in both samples are monocrystalline.

Temperature-programmed reduction (TPR) profiles for the calcined precursors are shown in Figure 3, while the temperatures at the maximum H₂ consumption (T_{MAX}) are summarized in Table 1. The Cu/SiO₂-I TPR profile (Figure 3, curve 1) showed a H₂ consumption peak centered at 614 K that can be assigned to the reduction of CuO large particles with low interaction with SiO₂ surface. The small and broad peak observed from 550 to 770 K can be ascribed to the reduction of a CuO phase minor fraction with a wide-ranging particle size distribution. In the case of Cu/SiO₂-PD (Figure 3, curve 2), a peak with a maximum at 566 K and a small shoulder at 590 K were detected, which may be due to the reduction of CuO with different particle size distributions and/or varying Cu-support interactions [37]. In this sense, other authors have suggested that, for Cu catalysts prepared by the precipitation–deposition method, a copper phyllosilicates phase is formed in addition to the CuO phase [38,39]. Therefore, the major peak at 566 K can be assigned to the reduction of a highly dispersed CuO phase, while the shoulder at 590 K to the reduction of copper phyllosilicates formed during the precipitation–deposition stage. In previous studies, our research group has shown that the reducibility of the CuO species increases with the diminution in particle size and the increasing Cu-support interaction that favors high copper dispersion [34,36]. Thus, it is reasonable that Cu/SiO₂-PD showed higher reducibility than Cu/SiO₂-I, due to the smaller size of CuO particles, in agreement with XRD and N₂O chemisorption results. The Cu/Al₂O₃-I TPR profile (Figure 3, curve 3) presented three H₂ consumption peaks; two main peaks at 512 and 580 K and a very small broad peak centered at 680 K. For Cu/Al₂O₃-I supported catalysts, Bridier et al. suggested that the first two peaks are due to the CuO reduction in two steps: CuO to Cu₂O at 512 K and Cu₂O to Cu⁰ at 580 K [40]. The areas of both peaks are similar, i.e., the H₂ consumption is practically the same, which is in agreement with the stoichiometry of the two proposed reduction steps. This explanation reinforces the above assignment for the TPR profile of CuO-supported on Al₂O₃ and is congruent with the fact that the Cu/Al₂O₃-I catalyst is constituted by large CuO particles interacting with the Al₂O₃ surface. The small and broad peak observed at 680 K may be attributed to the reduction of a very small fraction of surface copper aluminate [35]. Finally, in the CuMgAl, only one narrow H₂ consumption peak at 518 K was observed (Figure 3, curve 4), which was assigned to the reduction of Cu²⁺ highly dispersed both in the bulk and the surface of a non-stoichiometric magnesium aluminate [29]. In summary, the following reducibility pattern was obtained:

$\text{Cu/SiO}_2\text{-I} < \text{Cu/Al}_2\text{O}_3\text{-I} < \text{Cu/SiO}_2\text{-PD} < \text{CuMgAl}$, which was explained in function of particle size distribution and copper-support interactions.

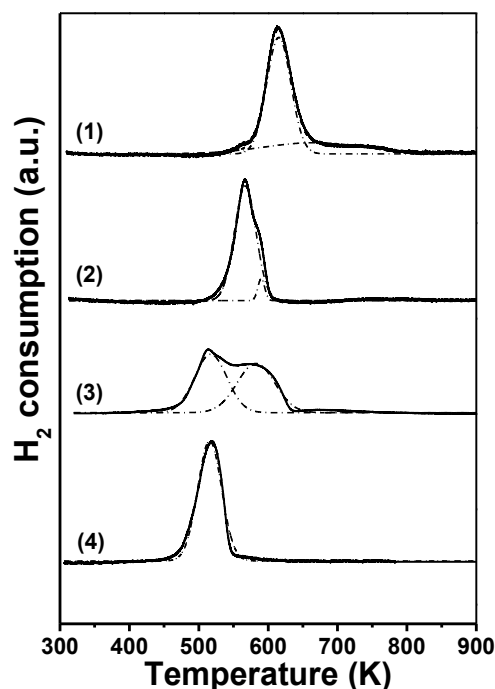


Figure 3. TPR profiles of calcined oxide precursors prepared in this work (H_2 (5%)/Ar; $60 \text{ cm}^3 \cdot \text{min}^{-1}$; $10 \text{ K} \cdot \text{min}^{-1}$): (1) Cu/SiO₂-I, (2) Cu/SiO₂-PD, (3) Cu/Al₂O₃-I, (4) CuMgAl.

The temperature-programmed desorption (TPD) profiles of NH₃, for both the unmodified supports and the samples of supported reduced copper, are shown in Figure 4, while the outcomes of the surface acid site concentrations are summarized in Table 1. The assessment of acid sites strength distribution was performed according to the NH₃ desorption temperature, taking the work of Shao et al. as reference [41]. Thus, ammonia desorption at temperatures below 523 K was attributed to its interaction with sites of low acid strength, while desorption between 523 and 673 K was assigned to sites with medium acid strength and above 673 K to strong acid sites. The CuMgAl sample presented the highest total acid sites concentration ($230 \mu\text{mol/g}^{-1}$) of the catalyst series prepared in this work and a very wide acid strength distribution. Figure 4 (curve 1) shows a peak at 490 K corresponding to weak strength acidity, but the major concentration of acid sites corresponds to moderate and strong acidity, with a maximum desorption temperature at 700 K. The NH₃-TPD profile of Cu/Al₂O₃-I, with a surface concentration of total acid sites of $81 \mu\text{mol/g}^{-1}$, approximately three times lower than CuMgAl, is presented in Figure 4, curve 2. This sample also presented a wide acidity distribution and the broad peak obtained could be deconvoluted in up to four peaks with maxima at 473, 530, 630 and 753 K. For Cu/Al₂O₃-I, the main NH₃ desorption peaks are at temperatures lower than 673 K, which means that the surface acid sites in higher concentration are those of low and moderate acidity, while the ones of high acid strength are in much lower concentrations. When Cu/Al₂O₃-I is compared with the unmodified Al₂O₃, whose total surface acid concentration is $61 \mu\text{mol/g}^{-1}$, it seems that incorporation of copper on the support produces an increase in the surface acid sites concentration, possibly due to the cupric ions that were not reduced under H₂ flow at 573 K. When compared to the TPD of SiO₂ (Figure 4, curve 6), the NH₃-TPD profile of the Cu-SiO₂-PD sample (Figure 4, curve 4) showed a considerable increase in the total acid site concentration from 6.5 to $68 \mu\text{mol/g}^{-1}$ (Table 1). This increase was more important for the weak and moderate acidity sites and could also be associated with the presence of Cu²⁺ ions, as a consequence of an incomplete reduction of the calcined sample. The NH₃-TPD profile of Cu/SiO₂-I (Figure 4, curve 5) showed a broad and small peak centered

at 515 K with a shoulder at 580 K. These can also be associated with an increase in surface site concentration of weak and moderate acidity with respect to unmodified SiO₂ due to the presence of surface copper cations. However, the increase in total acid site concentration in Cu/SiO₂-I was much lower than that for Cu/SiO₂-PD, in agreement with the low metallic dispersion of the former.

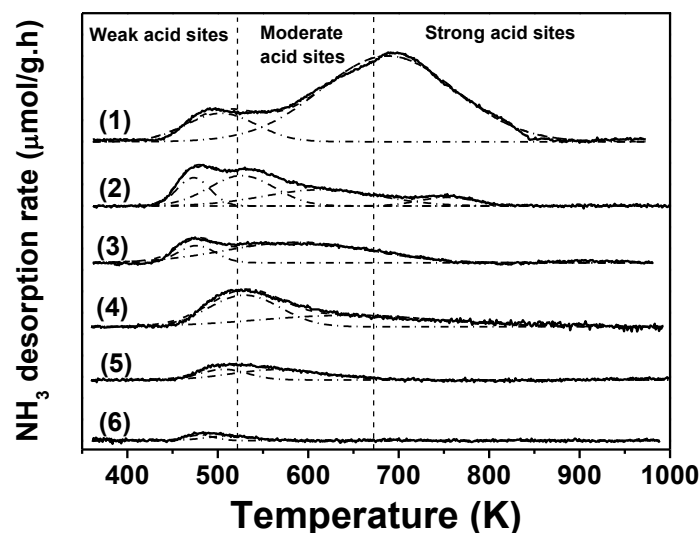


Figure 4. NH₃-TPD profiles of the calcined supports and reduced Cu-based samples: (1) CuMgAl, (2) Cu/Al₂O₃-I, (3) Al₂O₃, (4) Cu/SiO₂-PD, (5) Cu/SiO₂-I, (6) SiO₂.

The FTIR spectra of chemisorbed pyridine (Figure 5) back the assumptions coming from the NH₃-TPD results. In the case of the reduced Cu/Al₂O₃-I sample, only absorption infrared bands that can be assigned to pyridine chemisorbed on Lewis sites (1448–1450 and 1609 cm⁻¹) and H-bonded pyridine (1576 and 1593 cm⁻¹) were detected (Figure 5). No signals due to pyridine interaction with Brönsted acid sites (around 1530–1550 cm⁻¹ or at wavenumbers higher than 1630 cm⁻¹) were detected [42,43]. A similar spectrum was obtained for calcined Al₂O₃, i.e., only signals due to Lewis and H-bonded pyridine were observed (results not shown). FTIR spectra of chemisorbed pyridine over Cu/SiO₂-PD showed mainly absorption bands at 1448 and 1609 cm⁻¹, which are attributed to pyridine chemisorbed on Lewis acid sites [42]. The intensity of these peaks diminishes with evacuation temperature with a trend comparable to that of pyridine chemisorbed on the Cu/Al₂O₃-I surface, indicating that Lewis acidity is similar in both samples (Figure 5). When reduced Cu/SiO₂-I sample was contacted with pyridine in the gas phase, no signal was detected after evacuation at 303 K (Figure 5). An almost identical behavior was observed for the calcined SiO₂ support sample (not shown). These results are in agreement with NH₃-TPD, since total concentration and strength of surface acid sites on Cu/Al₂O₃-I and Cu/SiO₂-PD are rather similar, while they are higher on Cu/SiO₂-PD than on Cu/SiO₂-I. Therefore, we concluded that copper incorporation on the silica surface by precipitation–deposition at controlled pH produces an increase in the concentration and strength of surface Lewis acid sites, which is due to Cu²⁺ ions that cannot be reduced under the conditions used in this work. Finally, only Lewis acid sites were detected on the surface of the reduced CuMgAl surface (not shown), in agreement with results reported in previous works [43]. In summary, the FTIR of chemisorbed pyridine indicates that the total surface acidity of all of the reduced samples prepared in this work is mainly due to Lewis-type acid sites. In general terms, the surface concentration of Lewis acid sites and the acidity followed the trend: CuMgAl > Cu/Al₂O₃-I ≈ Cu/SiO₂-PD > Cu/SiO₂-I.

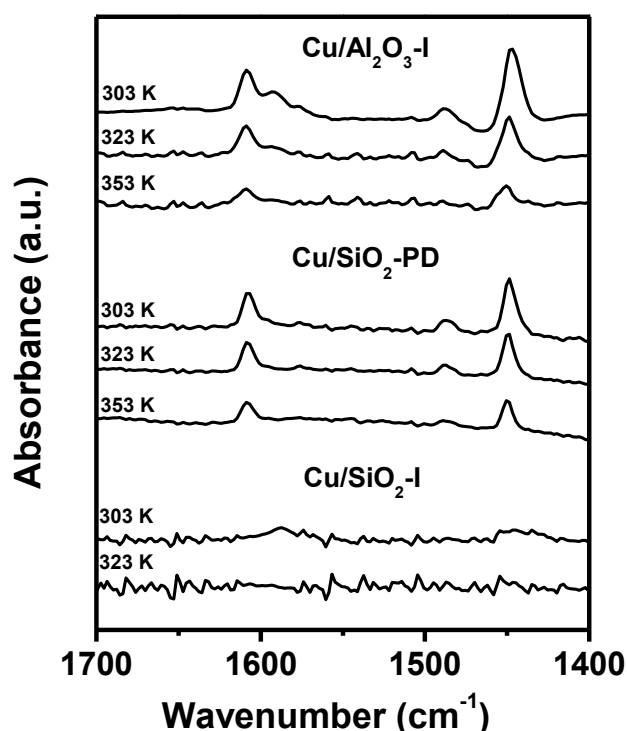


Figure 5. FTIR spectra of chemisorbed pyridine at different evacuation temperatures on the reduced Cu—based samples.

The reduced copper samples were also characterized by XPS, and the results are summarized in Table 2. In all cases, the peak corresponding to Cu 2p 3/2 can be satisfactorily fitted by deconvolution into two peaks (Figures S1–S3): the one between 932.0 and 933.7 eV, assigned to metallic copper, and that between 934.6 and 935.8 eV, attributed to Cu²⁺ species [44]. This confirms the assumption that part of the Cu²⁺ ions cannot be reduced in the conditions used in this work, probably because a fraction of them is stabilized by interaction with the support. Furthermore, as the Cu²⁺/(Cu⁰+Cu²⁺) increases, the binding energy shifts to higher values, in agreement with the possibility that Cu²⁺ ions and metallic copper particles are strongly interacting. As a consequence, Cu⁰ becomes deficient electronically, and therefore, the binding energy increases. An additional contribution to this shift may occur in Cu/Al₂O₃-I and CuMgAl by the interaction of metallic copper with Mg²⁺ and Al³⁺ ions of the corresponding matrixes. In the case of Mg, Al and Si, the absence of M-M signals (M=Mg, Al, Si) in the XPS spectra of the reduced samples (Table 2, Figures S1–S3) was verified. In the case of Si and Mg, only signals attributed to Mg-O, at 50.0 eV, and Si-O, around 103.5–103.7, were observed [45,46]. Instead, signals that can be assigned to both Al-O and Al-OH were observed in Cu/Al₂O₃-I and CuMgAl samples [45]. These results are in agreement with those obtained by FTIR of chemisorbed pyridine, and they support the assumption that the Lewis acid sites on the Cu/SiO₂-PD surface are due to the presence of Cu²⁺ ions strongly interacting with the support [39]. In Cu/Al₂O₃-I and CuMgAl, additional Lewis acid sites may be due to Al³⁺ and Mg²⁺ ions, present in magnesium aluminate and alumina surfaces [43].

In summary, the physicochemical characterization of the copper-based catalysts prepared in this work shows that their textural, structural, physical and chemical properties depend on the preparation methods and the supports used. A very well-dispersed phase of metallic nanoparticles 4 nm in size was attained, through the calcination and subsequent reduction under H₂ flow, from a copper-hydrated precursor deposited on a high-surface SiO₂ by precipitation at controlled pH. Instead, with the same support, the metallic phase produced from a precursor prepared by incipient wetness impregnation was constituted by larger metal copper particles with lower dispersion. In line with these results, a metallic

phase formed by large copper particles was obtained by incipient wetness impregnation over Al_2O_3 , while a highly dispersed metallic phase of copper nanoparticles was produced in the CuMgAl prepared by coprecipitation at constant pH.

Table 2. Main XPS spectral lines of the reduced samples and relative surface concentrations of Cu^{2+} .

Sample	Binding Energy (eV)					$\text{Cu}^{2+}/(\text{Cu}^0+\text{Cu}^{2+})$	
	Cu 2p 3/2		Mg 2p	Al 2p			Si 2p
	Cu^0	Cu^{2+}	Mg-O	Al-O	Al-OH		Si-O
Cu/SiO ₂ -I	932.0	934.6	-	-	-	103.7	0.08
Cu/SiO ₂ -PD	932.6	935.0	-	-	-	103.5	0.13
Cu/Al ₂ O ₃ -I	933.7	935.3	-	75.0	76.4	-	0.21
CuMgAl	933.7	935.8	50.0	74.4	77.1	-	0.22

As well, both the reducibility of oxidize supported-copper species and the sample acidity vary with the support and preparation method. As the interaction copper-support increases, the acidity and concentration of the surface acid sites rise as well. Thus, the highest acidity and concentration of surface acid sites was reached with CuMgAl and, to a lesser degree, with Cu/Al₂O₃. In addition, Cu/SiO₂-PD showed a higher concentration of surface acid sites than Cu/SiO₂-I. FTIR spectra of chemisorbed pyridine showed that the main surface acid sites in all of the samples are Lewis type. On the other hand, as the copper-support interaction augments, the particle size of oxidize copper species diminishes and thus does its reducibility.

2.2. Catalytic Tests

2.2.1. Performance of Cu-Based Catalysts

The Cu-based catalysts were evaluated in the liquid-phase HMF hydrogenation in a three-phase slurry reactor at 393 K and 15 bar of H₂ pressure, using THF as solvent. The rise of HMF conversion (X_{HMF}) as a function of $(W_{\text{Cu}} \cdot t)/n_{\text{HMF}}^0$ is shown in Figure 6. The initial hydrogenation rates (r_{HMF}^0 , mol/h⁻¹ · g_{Cu}⁻¹) and turnover frequencies (TOF, h⁻¹) are summarized in Table 3. The HMF conversion varied linearly with time when Cu/Al₂O₃-I was used as a catalyst, indicating that the global order with respect to HMF is zero (Figure 6). On the contrary, a non-linear change of HMF conversion with time was observed when the reaction was carried out with Cu/SiO₂-PD and CuMgAl. No HMF hydrogenation was detected with the Cu/SiO₂-I sample in the conditions used in this work. In summary, the pattern obtained for the initial hydrogenation rates was the following: Cu/SiO₂-PD ≈ CuMgAl > Cu/Al₂O₃-I >> Cu/SiO₂-I. The initial hydrogenation rate reached with Cu/Al₂O₃-I was approximately three to four times lower than those with CuMgAl and Cu/SiO₂-PD. On the other hand, the initial hydrogenation rate with CuMgAl was similar to that with Cu/SiO₂-PD, but after just 30 min, it diminished drastically, probably due to a rapid deactivation of the metallic copper phase. Instead, Cu/SiO₂-PD appears to be the most stable of the catalyst series used in this work. The catalytic activity and stability of Cu/SiO₂-PD can be attributed to the metallic phase composed of copper nanoparticles (3–4 nm in size) evenly dispersed over the silica surface [34]. These results are in agreement with the proposal of Zhu et al. [29], who showed that with the decrease in Cu particle size, the catalytic activity in HMF hydrogenation increases. This also explains the high initial activity observed for CuMgAl, in which the metallic phase is also composed of small copper particles. Conversely, Cu/SiO₂-I was not active, probably because the metallic phase is formed by large metallic Cu particles (>30 nm). However, Cu/Al₂O₃-I with a similar copper particle size as Cu/SiO₂-I showed significant activity in HMF hydrogenation. Possibly, in addition to the metal particle size, the copper-support interaction and/or the surface acidity of the catalyst play an important role in the catalytic activity. Therefore, these results indicate that the preparation method and the support nature have

an important influence on the physicochemical characteristics of the metallic copper phase and, consequently, on its catalytic performance in the liquid-phase HMF hydrogenation.

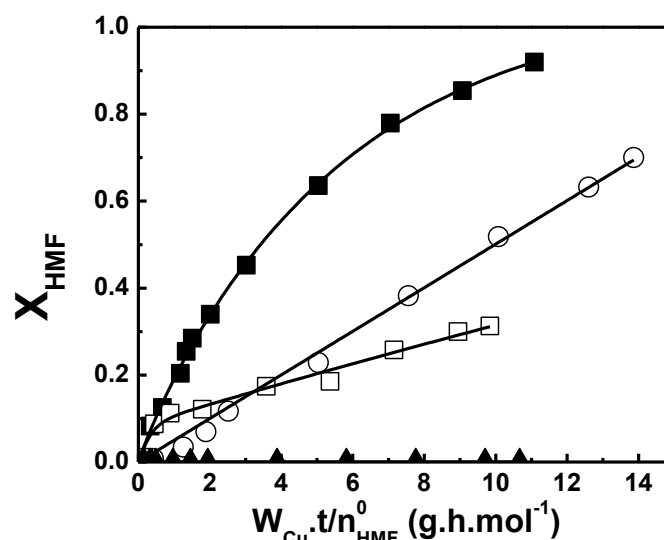


Figure 6. Conversion (X_{HMF}) as a function of $W_{Cu} \cdot t / n_{HMF}^0$ in the liquid-phase hydrogenation of HMF on Cu-based catalysts ($T = 393$ K, $P_{H_2} = 15$ bar, $C_{HFM}^0 = 0.13$ M, $V_{SOLV} = 150$ mL of THF). ■ Cu/SiO₂-PD, □ CuMgAl, ○ Cu/Al₂O₃-I, ▲ Cu/SiO₂-I.

Taking into account the differences in Cu dispersion, metallic load and surface acidity among the prepared samples, TOF values were estimated to compare the intrinsic activity of metal Cu sites. CuMgAl reached the highest TOF (1366 h⁻¹), which has the highest acidity and a high metallic copper dispersion. Cu/SiO₂-PD exhibited an intermediate TOF (650 h⁻¹), approximately three times higher than the TOF of Cu/Al₂O₃-I (198 h⁻¹). These results suggest that it is possible to obtain a highly dispersed metallic phase on an acid support surface, very active in HMF hydrogenation, when the catalyst precursors are prepared by precipitation methods at controlled pH. However, despite the high initial activity, the HMF conversion achieved with CuMgAl after 5.5 h of reaction was only 33%, indicating that rapid deactivation of metallic Cu phase took place. Among the possible causes of deactivation, one might be a rapid and strong adsorption of HMF and/or reaction products on the acid sites present on the CuMgAl surface. Taking into account the strength of the acid sites on the CuMgAl surface, the deactivation due to small amounts of humin produced from HMF must not be discarded [24–26]. Instead, after the same time of reaction, 91% and 70% HMF conversion was reached with Cu/SiO₂-PD and Cu/Al₂O₃-I catalysts, respectively (Table 3). These two catalysts have similar acidity and are lesser to that of CuMgAl.

Table 3. Liquid-phase HMF hydrogenation over Cu-based catalysts at 393 K and 15 bar H₂ pressure ($W_{Cat.} = 0.5$ g, $V_{THF} = 150$ mL of THF).

Catalysts	r_{HMF}^0 ^a (mol/g _{cu} ⁻¹ /h ⁻¹)	TOF ^b (h ⁻¹)	X_{HMF} ^c (%)	Y_{BHMF} ^d (%)	S_{BHMF} ^e (%)	CB ^f (%)	C ^g (wt%)
Cu/SiO ₂ -I	-	-	-	-	-	-	2.4
Cu/SiO ₂ -PD	0.182	650	91	89	98	99	3.2
Cu/Al ₂ O ₃ -I	0.05	198	70	68	97	98	5.7
CuMgAl	0.164	1366	33	32	96	98	7.4

^a Initial conversion rate of HMF hydrogenation. ^b Turnover frequency. ^c HMF conversion after 5.5 h reaction. ^d Yield in BHMF after 5.5 h reaction. ^e Selectivity to BHMF at 20% of HMF conversion. ^f Carbon Balance. ^g Amounts of carbonaceous residues determined by TPO.

In all of the cases, only one product was detected by chromatographic analysis, which is expected to be BHMF. In order to identify the product obtained during the liquid-phase HMF hydrogenation, the reaction mixture was purified by distillation and analyzed by

proton nuclear magnetic resonance, $^1\text{H-NMR}$ (Figure S4), infrared Fourier transform spectroscopy, FTIR (Figure S5), and gas chromatography–mass spectroscopy, GC-MS (Figure S6). $^1\text{H-NMR}$ analysis showed two signals at 4.42 and 6.22 ppm that can be assigned to the CH (s, 2H) and CH_2 (s, 4H) groups present in the BHMF molecule, in agreement with values reported in previous works [47,48]. No signal attributable to the CH_3 group was observed in the $^1\text{H-NMR}$ spectrum (Figure S4). The infrared spectrum showed several peaks in the $600\text{--}1600\text{ cm}^{-1}$ region that may be attributed to vibrations of BHMF molecules (Figure S5). The absorption bands at 756 , 820 and 975 cm^{-1} can be assigned to furan ring bending motion, while those at 1462 and 1560 cm^{-1} may come from the bending vibration of the CH_2 group and the C=C stretching of the furanic ring, respectively. In the $2800\text{--}3400\text{ cm}^{-1}$ region, a broad band at 3340 cm^{-1} due to the presence of hydroxyl groups was observed. The absorption bands at 2946 and 2877 cm^{-1} were attributed to stretching C-H of methylene groups ($-\text{CH}_2-$) [49]. The MS fragmentation spectra for the analyzed sample, shown in Figure S6, were similar to those reported by other authors for BHMF, whose molecular mass is 128 [48,50]. Therefore, the results obtained by $^1\text{H-NMR}$, FTIR and GC-MS confirm that the only product detected during the liquid-phase HMF hydrogenation over the copper-based catalyst is BHMF. Then, the trends for the yields in BHMF with time are similar to those of the HMF conversion. The highest yield in BHMF, after 5.5 h reaction, was reached with the Cu/SiO₂-PD catalyst, and it was around 90% at 91% HMF conversion (Table 3).

The selectivity to BHMF with Cu-based catalysts, active in the liquid-phase HMF hydrogenation, was always higher than 96%, and the carbon balance (CB) closed between 96 and 99%, but the catalytic activity on the C=O group hydrogenation varies with metallic particle size and surface acidity (Tables 1 and 3). The rate of the selective hydrogenation of the C=O group may be influenced by the surface acidity of the catalysts in two possible ways. On one hand, they could induce the adsorption and activation of HMF through its C=O group over the Lewis acid sites (Figure 5) that interact with the hydrogenating sites on the metallic copper nanoparticles [51]. On the other hand, the Cu atoms, constituting the metallic nanoparticles on the acidic surface, would become electron deficient due to charge transfer from the Cu atoms to the neighboring acid sites. Therefore, the adsorption of the electron-rich C=O group on the electron-deficient Cu atoms would also activate the carbonyl group for further hydrogenation [52,53].

In summary, all of the active copper-based catalysts used in this work were highly selective to BHMF, but the highest initial activity was obtained with those having the smallest metallic particle sizes, i.e., Cu/SiO₂-PD and CuMgAl catalysts. However, the hydrogenation rate decays very rapidly in the case of CuMgAl, probably due to deactivation of the highly dispersed metallic copper phase, and the final yield in BHMF was low.

In order to obtain information about possible causes for catalyst deactivation, analysis of the reaction mixture by atomic absorption spectroscopy (AAS) and temperature-programmed oxidation (TPO) measurements with all of the used catalysts were performed. As no evidence of cupric ions on the liquid phase after reaction was found, the metallic phase leaching was discarded as a possible cause of catalyst deactivation. The obtained TPO profiles are shown in Figure 7. It was found that the amount of carbonaceous residue deposited on the surface of each catalyst during reaction, in decreasing order, was the following: CuMgAl > Cu/Al₂O₃-I > Cu/SiO₂-PD > Cu/SiO₂-I (Table 3). The carbon load on the CuMgAl catalyst, at the end of the activity test, was approximately twice that of Cu/SiO₂-PD. These carbonaceous residues were burned in the range of 500 to 1000 K, which is in agreement with a strong interaction of these carbon compounds with a catalyst surface (Figure 7). In addition, CuMgAl showed the largest amount of carbonaceous residues in the temperature range of 500–750 K (Figure 7, curve 2) among all the catalysts used in this work, which is possibly due to the strong adsorption of HMF and/or product reactions on the surface of the non-stoichiometric spinel. These carbonaceous deposits could be partially covering the metallic Cu particles, contributing to the blocking of active sites in an irreversible way during reaction. The peak observed with a maximum at 960 K

can be attributed to the small amount of strongly chemisorbed carbon compounds on the acid and/or basic sites of the MgAl_2O_x surface. $\text{Cu}/\text{Al}_2\text{O}_3\text{-I}$ was the catalyst that followed CuMgAl in carbonaceous residues content (Figure 7, curve 1). The higher concentration of carbonaceous residues with respect to the silica-supported Cu catalysts is probably due to the fact that there are more acid sites on $\text{Cu}/\text{Al}_2\text{O}_3\text{-I}$ that favor the strong adsorption of HMF and/or other compounds on the catalyst surface. The TPO profile of the used $\text{Cu}/\text{SiO}_2\text{-PD}$ catalyst presents a signal at 536 K with a little shoulder at 680 K, while a similar TPO profile was observed for the used $\text{Cu}/\text{SiO}_2\text{-I}$ catalyst, but with a shift of 40 K to a higher temperature (Figure 7, curves 3 and 4). Furthermore, the amount of carbon compounds deposited on the catalyst surface is lower on $\text{Cu}/\text{SiO}_2\text{-I}$ than on $\text{Cu}/\text{SiO}_2\text{-PD}$ (Table 3). However, $\text{Cu}/\text{SiO}_2\text{-I}$ was not active in the HMF hydrogenation reaction, while $\text{Cu}/\text{SiO}_2\text{-PD}$ was the catalyst that reached the highest initial hydrogenation rate and the final HMF conversion and BHMF yield. If it is considered that the HMF molecules are rapidly and strongly chemisorbed on the surface of the large metallic particles of $\text{Cu}/\text{SiO}_2\text{-I}$, this could contribute to a very fast deactivation of the active phase from the very beginning of the reaction. As the metal surface exposed on $\text{Cu}/\text{SiO}_2\text{-I}$ is very low, the amount of HMF required to cover and deactivate the metal Cu sites would be small. Instead, the metallic copper dispersion on $\text{Cu}/\text{SiO}_2\text{-PD}$ is higher than that of $\text{Cu}/\text{SiO}_2\text{-I}$; therefore, the covering of metallic copper sites by carbonaceous species would affect the activity of the $\text{Cu}/\text{SiO}_2\text{-PD}$ catalyst to a lesser extent.

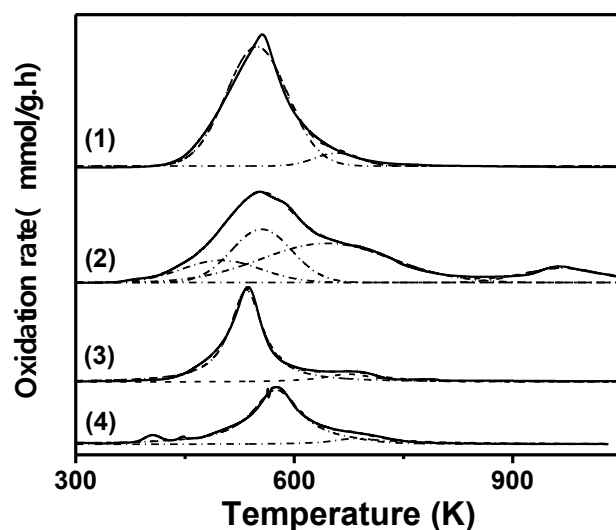


Figure 7. Temperature-programmed oxidation profiles of the used Cu-based catalyst. (1) $\text{Cu}/\text{Al}_2\text{O}_3\text{-I}$, (2) CuMgAl , (3) $\text{Cu}/\text{SiO}_2\text{-PD}$ (4) $\text{Cu}/\text{SiO}_2\text{-I}$ (O_2 (5%)/ N_2 ; $60 \text{ mL}/\text{min}^{-1}$; $10 \text{ K}/\text{min}^{-1}$).

These results lead to the conclusion that the strong chemisorption of reactant and/or product on the metallic surface could be a possible cause of the deactivation of the Cu-based catalysts. In order to confirm or reject this possible cause of deactivation, a series of activity tests and thermal treatments of the used $\text{Cu}/\text{SiO}_2\text{-PD}$ catalysts were carried out. The results are described in the following section.

2.2.2. Stability and Reuse Feasibility of the $\text{Cu}/\text{SiO}_2\text{-PD}$ Catalyst

The stability and reuse feasibility of the $\text{Cu}/\text{SiO}_2\text{-PD}$ catalyst, which showed the best catalytic performance of the catalyst series used in this work, was investigated (Figures 8 and 9, Table 4). The stability of $\text{Cu}/\text{SiO}_2\text{-PD}$ was analyzed by carrying out two consecutive catalytic tests. After 5.5 h reaction, the end of the first catalytic cycle (Figure 8, curve a), a conversion of HMF close to 95% was reached.

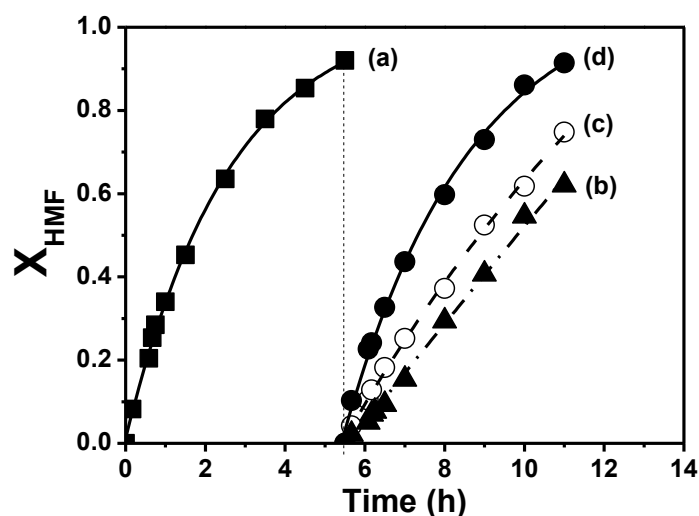


Figure 8. Catalytic performance of fresh, used and regenerated Cu/SiO₂-PD in the liquid-phase HMF hydrogenation at T = 393 K, P_{H₂} = 15 bar, C⁰_{HMF} = 0.13 M: (a) fresh catalyst, (b) used catalyst, (c) after H₂ treatment at 523 K, (d) after air treatment at 673 K and subsequent reduction in H₂ at 523 K.

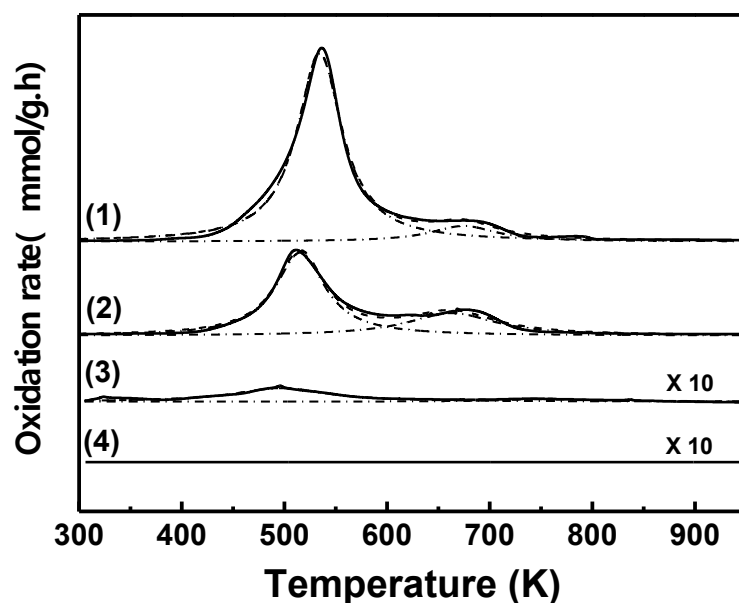


Figure 9. Temperature-programmed oxidation (TPO) profiles of Cu/SiO₂-PD catalyst. (1) Used catalyst; (2) after H₂ treatment at 523 K; (3) after air treatment at 673 K and subsequent reduction in H₂ at 523 K; (4) fresh catalyst (TPO experimental conditions: O₂ (5%)/N₂; 60 mL min⁻¹; 10 K min⁻¹).

Table 4. Liquid-phase HMF hydrogenation over fresh, used and regenerated Cu/SiO₂-PD catalyst. (T = 393 K, P_{H₂} = 15 bar, W_{Cat.} = 0.5 g and V_{Solv.} = 150 mL of THF).

Cu/SiO ₂ -PD Sample	r ⁰ _{HMF} ^a (mol/g _{cu} ⁻¹ /h ⁻¹)	X _{HMF} ^b (%)	%C ^c (wt%)	V _{HI} ^d × 10 ² (cm ³ /g ⁻¹)
Fresh catalyst	0.182	91	n.d.	6.72
Used catalyst	0.049	62	3.20	n.d.
H ₂ treated ^e	0.091	74	1.85	0.40
Air-H ₂ treated ^f	0.189	91	0.04	6.54

^a Initial conversion rate of HMF hydrogenation. ^b HMF conversion after 5.5 h of reaction. ^c Carbon amount determined from TPO profiles. ^d Volume of irreversibly chemisorbed hydrogen per gram of metallic Cu. ^e Used Cu/SiO₂-PD catalyst after treatment under H₂ flow. ^f Used Cu/SiO₂-PD catalyst after treatment under air and subsequent H₂ flow.

After the first reaction cycle, the system was cooled down to room temperature, and HMF was introduced into the reactor in order to recover the initial reactant concentration ($C_{HMF}^0 = 0.13$ M) in the liquid phase. Afterward, the catalytic performance was evaluated in a new cycle (Figure 8, curve b), and a linear trend for HMF conversion with reaction time was observed. In addition, it was determined that the initial hydrogenation rate in the second cycle was almost four times lower than that in the first cycle (Table 4). Furthermore, the HMF conversion at the end of the second cycle, i.e., after 5.5 h, was only 62% against the 95% reached in the first cycle. The important drops in the initial hydrogenation rate and final HMF conversion indicate that metallic Cu sites are being deactivated during HMF hydrogenation in liquid phase under the conditions used in this work.

Considering the loss of activity of Cu/SiO₂-PD after two consecutive catalytic tests, the feasibility of its reuse after a regeneration treatment was also investigated in this work. Following one cycle with fresh Cu/SiO₂-PD, the catalyst was recovered by filtration, dried at 343 K, reduced *ex situ* at 523 K in H₂ flow and finally reloaded into the reactor together with the necessary amount of HMF to re-establish the reactant initial concentration. The recovered catalyst was evaluated in a new catalytic cycle, under the same experimental conditions than those used for a fresh catalyst. A linear trend for the HMF conversion with time was obtained with the catalyst treated under H₂ flow, similar to that observed with the used and non-treated catalyst, (Figure 8, curves b,c). The latter indicates that the reaction would be order zero with respect to HMF as with a Cu/Al₂O₃-I catalyst. The initial reaction rate for the catalyst thermally treated under H₂ flow was 0.091 mol/h⁻¹/g_{Cu}⁻¹, which was almost twice higher than that obtained with the used and non-regenerated catalyst (Table 4). However, this hydrogenation rate was still lower than that obtained with the fresh catalyst, i.e., in the first catalytic cycle (Figure 8 curve a). Furthermore, the HMF conversion at the end of this cycle was only 74% (Table 4). In order to verify the feasibility of recovering the activity of the fresh catalyst, after the catalytic cycle with Cu/SiO₂-PD thermally treated with H₂, the catalyst was filtered, dried at 343 K and calcined in air at 673 K for 2 h. Afterward, it was reduced *ex situ* at 523 K in H₂ flow and reloaded into the reactor together with the necessary amount of HMF. It was verified that both the initial hydrogenation rate and the HMF conversion obtained with the fresh Cu/SiO₂-PD catalysts were recovered after this calcination–reduction treatment (Table 4). Furthermore, the progress of the HMF conversion as a function of time with both the fresh and regenerated catalyst was very similar (Figure 8, curves a,d).

In order to obtain more information about the reversibility of the deactivation process of Cu/SiO₂-PD, TPO and H₂ chemisorption, measurements were performed, and the main results are summarized in Figure 9 and Table 4. When the used Cu/SiO₂-PD sample was treated in hydrogen flow at 523 K, it was not enough to remove all the carbon adsorbed on the catalyst surface (Figure 9, curve 2), and more than half of the carbonaceous residues remained on the catalyst surface (Table 4). It is likely that the amount of carbonaceous residues remaining (1.85 wt%) was sufficient to partially block the metallic surface sites, and consequently, HMF hydrogenation was negatively affected. Instead, practically all the carbonaceous residues were removed from the used catalyst after calcination in air flow at 673 K (Table 4), and thus, no significant differences between the TPO profiles of the calcined and fresh CuSiO₂-PD catalyst were observed (Figure 9, curves 3 and 4). This result is in agreement with the recovery of the original catalytic activity after calcination of the used catalyst followed by reduction in H₂ flow (Figure 9 and Table 4). In addition, we found a linear correlation between the initial reaction rate and the carbon amount measured by TPO (Figure S7), in agreement with the proposal that the carbonaceous residues deposited on the surface catalyst must be the main cause for the deactivation of the Cu/SiO₂-PD catalyst. In this way, leaching can be ruled out as a possible cause of deactivation, since if part of the metallic phase had been lost, it would not have been feasible to recover the original catalytic activity of Cu/SiO₂-PD.

The measurements of hydrogen chemisorption capability of fresh, used, and regenerated samples of Cu/SiO₂-PD catalysts are also in good agreement with the above findings.

The volume of irreversibly chemisorbed hydrogen per gram of metallic Cu for the fresh catalyst was $6.7 \times 10^{-2} \text{ cm}^3/\text{g}^{-1}$, while no hydrogen chemisorption was detected with the used Cu/SiO₂-PD sample (Table 4). Furthermore, the volume of irreversibly chemisorbed hydrogen on the used Cu/SiO₂-PD catalyst after treatment in H₂ flow at 523 K was approximately twenty times smaller than that of the fresh catalyst (Table 4). It is possible that the very low hydrogen chemisorption capacity is a consequence of the partial covering of the metallic Cu surface by the deposits of carbonaceous residues. Instead, the used Cu/SiO₂-PD catalyst, after calcination in air flow at 673 K and subsequent reduction in H₂ flow at 523 K, showed a similar capability for irreversible hydrogen chemisorption to that of the fresh catalyst. This result is in agreement with the total removal of the carbonaceous residues from the catalytic surface, as it was determined by TPO. Therefore, it is possible to re-obtain the H₂ chemisorption capability and the original activity of the fresh Cu/SiO₂-PD catalyst by a combined thermal treatment of the used catalyst, carried out in two steps: thermal treatment in air at 673 K and subsequent reduction under H₂ flow at 523 K. This treatment helps to clean the metallic Cu phase by whole removal of the carbonaceous residues deposited during the liquid-phase HMF hydrogenation.

In summary, it can be asserted that the deactivation of Cu/SiO₂-PD would be mainly due to blocking of the metallic copper phase by carbonaceous residues, probably HMF and/or BHMF strongly adsorbed on the metal active sites. The total removal of carbonaceous surface residues from the Cu/SiO₂-PD surface and the recovery of the original catalytic activity can be reached by a thermal treatment in air followed by reduction under H₂ flow.

3. Materials and Methods

3.1. Catalyst Preparation

Cu-based catalysts were prepared by different methods: incipient wetness impregnation, precipitation–deposition and co-precipitation. Cu/SiO₂-I and Cu/Al₂O₃-I catalyst precursors were prepared using the incipient wetness impregnation method over commercial SiO₂ (Sigma-Aldrich, Buenos Aires, Argentina) and γ -Al₂O₃ (Ketjen CK 300, Amsterdam, Netherlands), respectively. The supports were impregnated with an adequate amount of a Cu(NO₃)₂·3H₂O (Merck 98%, Buenos Aires, Argentina) aqueous solution, prepared using mili-Q[®] purified water, dried in an oven at 373 K for 12 h, and finally calcined in air flow at 673 K for 4 h.

Cu/SiO₂-PD catalyst was prepared by the precipitation–deposition method at controlled pH, by simultaneously adding dropwise aqueous solutions of Cu(NO₃)₂·3H₂O and K₂CO₃ to a SiO₂ stirred suspension in mili-Q[®] purified water. Over the preparation, the pH solution was monitored and maintained at 7.2 ± 0.2 while the temperature was set to 338 K and controlled by using a thermostatic water bath. The hydrated precursor thus obtained was separated by filtration, washed with deionized water and dried at 358 K overnight. Finally, it was calcined in air flow at 673 K for 4 h [34,35].

The hydrated precursor of the CuMgAl catalyst was prepared by the co-precipitation method at 338 K, keeping the pH at 10.0 ± 0.2 , following the procedure described elsewhere [36,54]. The precipitate obtained was separated by filtration, washed with deionized water at 338 K and dried at 353 K overnight. Finally, the hydrated precursor was thermally decomposed in N₂ flow at 773 K for 5 h to obtain the corresponding mixed oxide.

3.2. Catalyst Characterization

Cu loading of the calcined samples was determined by atomic absorption spectroscopy (AAS) using a Perkin-Elmer, (Massachusetts, United States) 3110 spectrometer. The specific surface area (S_g) and pore volume (V_g) of the samples were measured by N₂ physisorption at 77 K in a Quantachrome Autosorb I sorptometer.

The identification of polycrystalline species in the oxide precursors (calcined samples) and the samples reduced in hydrogen flow and passivated in O₂ (1%)/N₂ flow at room temperature were carried out by X-ray diffraction (XRD) employing an Empyrean

Series 2 X-ray system (Panalytical, Malvern, England), with Ni-filtered Cu-K α radiation ($\lambda = 0.1540$ nm) and $2^\circ/\text{min}^{-1}$ scan speed. The average crystallite size of calcined and reduced samples was estimated applying Scherrer's equation.

Temperature-programmed reduction (TPR) profiles of the oxide precursors were obtained in H₂ (5%)/Ar flow ($60\text{ cm}^3/\text{min}^{-1}$) using a Hiden Analytical QGA (Warrington, England) system equipped with quadrupole mass analyzer.

The Cu metal dispersion was determined by pulse titration with N₂O at 363 K and considering a stoichiometry Cu_s⁰/N₂O = 2, where Cu_s⁰ indicates the superficial atoms of metal copper [55]. The reactor effluent during the pulse titration was analyzed by mass spectroscopy (MS) using a Balzers Omnistar (Pfeiffer Vacuum, Asslar, Germany) unit. Previously to titration, the samples were reduced in situ for 2 h by flowing H₂ (100%) through the reactor.

The concentration and strength of surface acid sites were determined by temperature-programmed desorption of NH₃ (NH₃-TPD). The samples were reduced in situ with H₂ (100%) flow for 2 h at the corresponding temperature of reduction. Next, the system was cooled down to 373 K in H₂ flow, flushed with He flow and then exposed to an NH₃ (1%)/He stream at 373 K for 1 h. The physisorbed NH₃ was removed in He flow at 373 K for 0.5 h. Finally, the temperature was raised from 373 to 973 K at $10\text{ K}/\text{min}^{-1}$ in He ($60\text{ cm}^3/\text{min}^{-1}$) flow, and the NH₃ concentration in the effluent was measured by mass spectroscopy (MS) using a Balzers Omnistar (Pfeiffer Vacuum, Asslar, Germany) unit.

The nature of surface acid sites was determined by Fourier transform infrared spectroscopy (FTIR) using a Shimadzu IRPrestige-21 spectrophotometer (Kyoto, Japan) and pyridine as probe molecule. The samples were prepared by mixing 15 mg of reduced catalyst with 15 mg of KBr under a pressure of 2 toncm^{-2} . The pellet thus obtained was transferred into the IR cell. All the samples were treated under vacuum (0.013 Pa) at 673 K for 1 h, and then, a background spectrum was recorded after cooling the sample at room temperature. Subsequently, pyridine was injected into the IR cell, and spectra of the chemisorbed pyridine after evacuation at different temperatures between 303 and 423 K were collected.

Hydrogen chemisorption was measured via volumetric adsorption experiments in the pressure range 0–0.15 bar applying the double isotherm method, as described elsewhere [51]. The Cu/SiO₂-PD samples were reduced in situ with H₂ (100%) at 523 K for 2 h and then evacuated at 10^{-7} bar for 2 h, while the used sample was reduced at 423 K for 15 min and then evacuated at 10^{-7} bar for 2 h. The amount of chemisorbed hydrogen was calculated as the difference between the total and the physisorbed H₂.

X-ray photoelectron spectroscopy (XPS) experiments were carried out in a SPECS multi-analysis device with a dual Mg/Al X-ray source and a PHOIBOS150 hemispherical analyzer. Before measurements, the reduced-passivated samples were placed in the analyzer chamber and treated in situ with H₂ (5%)/Ar at the corresponding reduction temperature and then evacuated for 2 h under ultra-high vacuum (UHV) (10^{-9} mbar). Spectra were obtained using MgK α radiation, and data were processed using CasaXPS version 2.3.16 software.

Temperature-programmed oxidation (TPO) profiles of fresh, used and regenerated Cu-based catalysts were obtained in a flow set-up by heating the sample from room temperature to 980 K, at $10\text{ K}/\text{min}^{-1}$ in O₂ (1%)/N₂ gas stream. The evolved CO₂ was completely converted to CH₄ in a methanator using a Ni (40%)/Kieselghur (Sigma.Aldrich, Buenos Aires, Argentina) catalyst at 673 K. The methanator outlet was monitored using a flame ionization detector (FID), and data acquisition was carried out by using Peak 356 software. For carbon content quantification, a calibration was made with a pattern catalyst standard sample having a previously determined known amount of coke carbon.

3.3. Catalytic Tests

The liquid-phase catalytic hydrogenation of HMF (AVA Biochem, purity $\geq 99\%$) was carried out in a 500 mL stainless steel autoclave at 393 K and 15 bar of H₂ pressure, using

150 mL of tetrahydrofuran (Cicarelli, pro-analysis +99.0%, San Lorenzo, Argentina) as solvent. Prior to the catalytic tests, the oxide precursors (0.5 g) were reduced *ex situ* in H₂ (100%) flow (60 mL/min⁻¹) for 2 h at the reduction temperature close to the maximum H₂ consumption obtained from the TPR profiles, then cooled down in hydrogen flow and finally transferred to the high-pressure reactor under inert atmosphere (N₂). Next, 2.5 g of HMF and 1 mL of hexadecane (internal standard) were added into the reactor. Afterward, the system was purged and pressurized with 1 bar of N₂. Next, the reaction mixture was stirred at 760 rpm and heated to the reaction temperature at 5 K/min⁻¹. Finally, when the reaction temperature was reached, the total pressure was increased with H₂ to the preset reaction pressure value.

Liquid samples were withdrawn from the reactor at regular time intervals to monitor the progress of reaction. Sampling was carried out in a system that allows for the extraction of small volumes of liquid, so as to extract less than 3% of the total liquid volume throughout the process. In addition, this system avoids the flash vaporization of the samples due to the abrupt decompression from the pressure inside the reactor to atmospheric pressure. Off-line analysis of these samples was performed employing gas chromatography in a Shimadzu 2014 GC chromatograph equipped with an ALPHA DEXTM 120 column (30 m × 0.25 mm × 0.25 μm film thickness) and a flame ionization detector.

The HMF conversion was calculated as $X_{HMF} = (n_{HMF}^0 - n_{HMF}) / n_{HMF}^0$, where n_{HMF}^0 is the initial HMF moles, and n_{HMF} is the HMF moles at a given reaction time. The product yield (Y_j) was calculated as $Y_j = v_{HMF} \cdot n_j / v_j \cdot n_{HMF}^0$, where n_j is the moles of product j and v_{HMF} and v_j are the stoichiometric factors of HMF and product j , respectively, both equal to the unity. Selectivity to product j (S_j) was obtained as $S_j = \eta_j / X_{HMF}$. The carbon balance (CB) was defined as:

$$CB = (\alpha_{HMF} \cdot n_{HMF} + \alpha_{BHMF} \cdot n_{BHMF}) / (\alpha_{HMF} \cdot n_{HMF}^0) \quad (1)$$

where α_{HMF} and α_{BHMF} are the number of carbon atoms in HMF and BHMF, which is 6 for both molecules. Thus, the CB expression simplifies to:

$$CB = (n_{HMF} + n_{BHMF}) / n_{HMF}^0 \quad (2)$$

The initial rates of HMF hydrogenation (r_{HMF}^0 , mol_{HMF}/h⁻¹/g_{Cu}⁻¹) were estimated by applying polynomial differentiation on the conversion data as a function of $W \cdot t / n_{HMF}^0$ and evaluating the corresponding derivative at zero time, where W is the total metal weight (g_{Cu}) loaded to the reactor and t is time of reaction (h).

3.4. Product Characterization

Mass spectrometry analysis was carried out with a Thermo Scientific Trace 13000 spectrometer coupled with a Thermo Scientific Trace 1300 gas chromatograph equipped with a TR 5MS column (30 m × 0.25 mm × 0.25 μm film thickness).

¹H NMR measurements were performed in H₂O + D₂O (10%) using a BRUKER Avance 300 MHz spectrometer. Solvent signal suppression was performed using Bruker WATERSUP pulse sequence with an o1p at 4.7 ppm.

FTIR analysis of the final reaction mixture was conducted in a SHIMADZU FTIR-8201PC unit in the wavenumber range of 400–4000 cm⁻¹ (spectra resolution: 4 cm⁻¹, number of scans:40). For this purpose, 2 mg of sample was mixed with 100 mg of dry KBr, and the mixture was then ground into a fine powder before compressing into a disc.

4. Conclusions

A supported copper catalyst, obtained by the precipitation–deposition method over a high-surface silica (Cu/SiO₂-PD), was the most active and stable of the copper catalyst series used in this work for the selective hydrogenation of 5-hydroxymethylfurfural (HMF) to 2,5-bis(hydroxymethyl)furan (BHMF) in liquid phase, which is a reaction of industrial interest. This is because HMF is obtained from renewable sources, and BHMF is used in the

manufacture of polyurethane foams, which is a potential raw material for the production of biodegradable polyesters.

The active phase of Cu/SiO₂-PD is mainly formed by metallic copper nanoparticles that are evenly dispersed on a surface with medium acidity, which is due to Lewis acid sites from Cu²⁺ ions interacting with the support surface that cannot be reduced at the conditions used in this work. The metallic active phase was partially blocked during reaction by carbonaceous compounds that chemisorb strongly on the catalyst surface, which can be removed by a thermal treatment in air flow. The catalyst activity of Cu/SiO₂-PD was totally recovered after subsequent reduction under H₂ flow. Thus, we concluded that the reuse of this catalyst after each batch in the hydrogenation process is very feasible.

Cu/SiO₂-I prepared by the incipient wetness impregnation method, mainly constituted by large metal copper particles supported on the silica surface, was inactive for HMF hydrogenation. This is probably due to a very fast deactivation of the metallic copper sites by strong adsorption of the reactant molecules.

CuMgAl catalysts, prepared by coprecipitation, have surface acid sites interacting strongly with reactant and/or product molecules, which lead to an important deactivation of the metallic copper phase. As a consequence, total conversion of HMF was not reached during the catalytic tests that were carried out in this work.

In summary, a catalyst having good activity and stability in the liquid-phase selective hydrogenation of HMF to BHMF, which can be reused, was the one whose metallic copper phase is highly dispersed on a surface with low or medium acidity.

Supplementary Materials: The following supporting information can be downloaded at <https://www.mdpi.com/article/10.3390/catal12111476/s1>. Figure S1: X-ray photoelectron spectroscopy of reduced Cu/SiO₂-PD sample; Figure S2: X-ray photoelectron spectroscopy of reduced Cu/Al₂O₃-I sample; Figure S3: X-ray photoelectron spectroscopy of reduced CuMgAl sample; Figure S4: ¹H-NMR of BHMF (300 MHz, H₂O/D₂O (90:10), water suppression at 4.71 ppm); Figure S5: Infrared Fourier transform spectroscopy (FTIR) spectra of BHMF; Figure S6: Mass spectroscopy (MS) of BHMF; Figure S7: Initial hydrogenation rate (r_{HMF}^0) of HMF as a function of the percentage of carbonaceous residues (%C) deposited on Cu/SiO₂-PD.

Author Contributions: Methodology, J.Z., C.I.M., H.A.D. and A.M.; investigation, J.Z., C.I.M., H.A.D. and A.M.; data curation, J.Z. and C.I.M.; writing—original draft preparation, J.Z.; writing—review and editing C.I.M. and A.M.; supervision, A.M.; project administration, A.M. All authors have read and agreed to the published version of the manuscript.

Funding: This research was funded by CONICET (Consejo Nacional de Investigaciones Científicas y Técnicas), grant number PIP 2017-767, ANPCyT (Agencia Nacional de Promoción Científica y Tecnológica), grant number PICT 2015-1892 and UNL (Universidad Nacional del Litoral), grant number CAI+D 2020-50620190100066LI.

Data Availability Statement: Not applicable.

Acknowledgments: The authors thank Universidad Nacional del Litoral (UNL), Consejo Nacional de Investigaciones Científicas y Técnicas (CONICET), and Agencia Nacional de Promoción Científica y Tecnológica (ANPCyT), Argentina, for the financial support. Special thanks are given to ANPCyT for the purchase of the SPECS multitechnique analysis instrument (PME8-2003). As well, they thank Victoria Vaillard and Pablo Nieres for proton nuclear magnetic resonance (¹H-NMR) and infrared Fourier transform spectroscopy (FTIR) analyses. The authors especially thank MDPI for the invitation to publish in the Special Issue of Catalysts (MDPI)—Catalysis in Green Chemistry and Organic Synthesis.

Conflicts of Interest: The authors claim that there is no conflict of interest to declare.

References

1. Climent, M.J.; Corma, A.; Iborra, S. Heterogeneous Catalysts for the One-Pot Synthesis of Chemicals and Fine Chemicals. *Chem. Rev.* **2011**, *111*, 1072–1113. [[CrossRef](#)]
2. Corma, A.; Iborra, S.; Velty, A. Chemical Routes for the Transformation of Biomass into Chemicals. *Chem. Rev.* **2007**, *107*, 2411–2502. [[CrossRef](#)]
3. Mohan, S.V.; Nikhil, G.N.; Chiranjeevi, P.; Reddy, C.N.; Rohit, M.V.; Kumar, A.N.; Sarkar, O. Waste biorefinery models towards sustainable circular bioeconomy: Critical review and future perspectives. *Bioresour. Technol.* **2016**, *215*, 2–12. [[CrossRef](#)]
4. Huber, G.W.; Iborra, S.; Corma, A. Synthesis of Transportation Fuels from Biomass: Chemistry, Catalysts, and Engineering. *Chem. Rev.* **2006**, *106*, 4044–4098. [[CrossRef](#)] [[PubMed](#)]
5. Christensen, C.H.; Rass-Hansen, J.; Marsden, C.C.; Taarning, E.; Egeblad, K. The Renewable Chemicals Industry. *ChemSusChem* **2008**, *1*, 283–289. [[CrossRef](#)] [[PubMed](#)]
6. Rosenfeld, C.; Konnerth, J.; Sailer-Kronlachner, W.; Rosenau, T.; Potthast, A.; Solt, P.; van Herwijnen, H.W.G. Hydroxymethylfurfural and its Derivatives: Potential Key Reactants in Adhesives. *ChemSusChem* **2020**, *13*, 5408–5422. [[CrossRef](#)]
7. Galkin, K.; Ananikov, V. 5-Hydroxymethylfurfural, the “Sleeping Giant” of Sustainable Chemistry, Awaken? *ChemSusChem* **2019**, *12*, 2976–2982. [[CrossRef](#)] [[PubMed](#)]
8. Galkin, K.I.; Ananikov, V.P. The Increasing Value of Biomass: Moving from C6 Carbohydrates to Multifunctionalized Building Blocks via 5-(hydroxymethyl)furfural. *ChemSusChem* **2020**, *9*, 1135–1148. [[CrossRef](#)] [[PubMed](#)]
9. Leshkov, Y.; Barrett, C.; Liu, Z.; Dumesic, J. Production of dimethylfuran for liquid fuels from biomass-derived carbohydrates. *Nature* **2007**, *447*, 982–986. [[CrossRef](#)]
10. Saha, B.; Abu-Omar, M.M. Advances in 5-hydroxymethylfurfural production from biomass in biphasic solvents. *Green Chem.* **2014**, *16*, 24–38. [[CrossRef](#)]
11. Bicker, M.; Hirth, J.; Vogel, H. Dehydration of fructose to 5-hydroxymethylfurfural in sub- and supercritical acetone. *Green Chem.* **2003**, *5*, 280–284. [[CrossRef](#)]
12. Yu, I.K.M.; Tsang, D.C.W. Conversion of biomass to hydroxymethylfurfural: A review of catalytic systems and underlying mechanisms. *Bioresour. Technol.* **2017**, *238*, 716–732. [[CrossRef](#)]
13. Rosatella, A.A.; Simeonov, S.P.; Frade, R.F.M.; Afonso, C.A.M. 5-Hydroxymethylfurfural (HMF) as a building block platform: Biological properties, synthesis and synthetic applications. *Green Chem.* **2011**, *13*, 754–793. [[CrossRef](#)]
14. Guo, W.; Heeres, H.J.; Yue, J. Continuous synthesis of 5-hydroxymethylfurfural from glucose using a combination of AlCl₃ and HCl as catalyst in a biphasic slug flow capillary microreactor. *Chem. Eng. J.* **2020**, *381*, 122754. [[CrossRef](#)]
15. Moreau, C.; Belgacem, M.N.; Gandini, A. Recent Catalytic Advances in the Chemistry of Substituted Furans from Carbohydrates and in the Ensuing Polymers. *Top. Catal.* **2004**, *27*, 11–30. [[CrossRef](#)]
16. Pentz, W.J. Furan-Based Compounds and Composition Thereof. GB Patent, 131,014, 13 June 1984.
17. Cai, H.; Li, C.; Wang, A.; Zhang, T. Biomass into chemicals: One-pot production of furan-based diols from carbohydrates via tandem reactions. *Catal. Today* **2014**, *234*, 59–65. [[CrossRef](#)]
18. Zeng, C.; Seino, H.; Ren, J.; Hatanaka, K.; Yoshie, N. Bio-Based Furan Polymers with Self-Healing Ability. *Macromolecules* **2013**, *46*, 1794–1802. [[CrossRef](#)]
19. Zeng, C.; Seino, H.; Ren, J.; Hatanaka, K.; Yoshie, N. Self-healing bio-based furan polymers cross-linked with various bis-maleimides. *Polymer* **2013**, *54*, 5351–5357. [[CrossRef](#)]
20. Alamillo, R.; Tucker, M.; Chia, M.; Pagán-Torres, Y.; Dumesic, J. The selective hydrogenation of biomass-derived 5-hydroxymethylfurfural using heterogeneous catalysts. *Green Chem.* **2012**, *14*, 1413–1419. [[CrossRef](#)]
21. Zu, Y.; Yang, P.; Wang, J.; Liu, X.; Ren, J.; Lu, G.; Wang, Y. Efficient production of the liquid fuel 2,5-dimethylfuran from 5-hydroxymethylfurfural over Ru/Co₃O₄ catalyst. *Appl. Catal. B Environ.* **2014**, *146*, 244–248.
22. Jae, J.; Zheng, W.; Karim, A.M.; Guo, W.; Lobo, R.F.; Vlachos, D.G. The Role of Ru and RuO₂ in the Catalytic Transfer Hydrogenation of 5-Hydroxymethylfurfural for the Production of 2,5-Dimethylfuran. *ChemCatChem* **2014**, *6*, 848–856. [[CrossRef](#)]
23. Jae, J.; Zheng, W.Q.; Lobo, R.F.; Vlachos, D.G. Production of Dimethylfuran from Hydroxymethylfurfural through Catalytic Transfer Hydrogenation with Ruthenium Supported on Carbon. *ChemSusChem* **2013**, *6*, 1158–1162. [[CrossRef](#)]
24. Fulignatia, S.; Antonetta, C.; Wilbers, E.; Licursia, D.; Heeres, H.J.; Raspolli Galletta, A.G. Tunable HMF hydrogenation to furan diols in a flow reactor using Ru/C as catalyst. *J. Ind. Eng. Chem.* **2021**, *100*, 390.e1–390.e9.
25. Fulignatia, S.; Antonetta, C.; Tabanelli, T.; Fabrizio, C.; Raspolli Galletta, A.G. Integrated Cascade Process for the Catalytic Conversion of 5-Hydroxymethylfurfural to Furanic and Tetrahydrofuranic Diethers as Potential Biofuels. *ChemSusChem* **2022**, *15*, e202200241.
26. Fulignatia, S.; Antonetta, C.; Licursia, D.; Pieraccioni, M.; Wilbers, E.; Heeres, H.J.; Raspolli Galletta, A.G. Insight into the hydrogenation of pure and crude HMF to furan diols using Ru/C as catalyst. *Appl. Catal. A Gen.* **2019**, *578*, 122–133. [[CrossRef](#)]
27. Kong, X.; Zhu, Y.; Zhen, H.; Dong, F.; Zhu, Y.; Li, Y.W. Switchable synthesis of 2,5-dimethylfuran and 2,5-dihydroxymethyltetrahydrofuran from 5-hydroxymethylfurfural over Raney Ni catalyst. *RSC Adv.* **2014**, *4*, 60467–60472. [[CrossRef](#)]
28. Lima, S.; Chadwick, D.; Hellgardt, K. Towards sustainable hydrogenation of 5-(hydroxymethyl)furfural: A two-stage continuous process in aqueous media over RANEY® catalysts. *RSC Adv.* **2017**, *7*, 31401–31407. [[CrossRef](#)]

29. Zhu, Y.; Kong, X.; Zheng, H.; Ding, G.; Zhu, Y.; Li, Y.W. Efficient synthesis of 2,5-dihydroxymethylfuran and 2,5-dimethylfuran from 5-hydroxymethylfurfural using mineral-derived Cu catalysts as versatile catalysts. *Catal. Sci. Technol.* **2015**, *8*, 4208–4217. [[CrossRef](#)]
30. Upare, P.P.; Hwang, Y.K.; Hwang, D.W. An integrated process for the production of 2,5-dihydroxymethylfuran and its polymer from fructose. *Green Chem.* **2018**, *20*, 875–889. [[CrossRef](#)]
31. Hu, D.; Hu, H.; Zhou, H.; Li, G.; Chen, C.; Zhang, J.; Yang, Y.; Hu, Y.; Zhang, Y.; Wang, L. The effect of potassium on Cu/Al₂O₃ catalysts for the hydrogenation of 5-hydroxymethylfurfural to 2,5-bis(hydroxymethyl)furan in a fixed-bed reactor. *Catal. Sci. Technol.* **2018**, *8*, 6091–6099. [[CrossRef](#)]
32. Xiang, X.; Cui, J.; Ding, G.; Zheng, H.; Zhu, Y.; Li, Y. One-Step Continuous Conversion of Fructose to 2,5-Dihydroxymethylfuran and 2,5-Dimethylfuran. *ACS Sustain. Chem. Eng.* **2016**, *4*, 4506–4510. [[CrossRef](#)]
33. Wang, Q.; Feng, J.; Zheng, L.; Wang, B.; Bi, R.; He, Y.; Liu, H.; Li, D. Interfacial Structure-Determined Reaction Pathway and Selectivity for 5-(Hydroxymethyl)furfural Hydrogenation over Cu-Based Catalysts. *ACS Catal.* **2020**, *10*, 1353–1365. [[CrossRef](#)]
34. Zelin, J.; Meyer, C.I.; Regenhardt, S.A.; Sebastian, V.; Garetto, T.F.; Marchi, A.J. Selective liquid-phase hydrogenation of fructose to D-mannitol over copper-supported metallic nanoparticles. *Chem. Eng. J.* **2017**, *319*, 48–56. [[CrossRef](#)]
35. Zelin, J.; Regenhardt, S.A.; Meyer, C.I.; Duarte, H.A.; Sebastian, V.; Marchi, A.J. Selective aqueous-phase hydrogenation of D-fructose into D-mannitol using a highly efficient and reusable Cu-Ni/SiO₂ catalyst. *Chem. Eng. Sci.* **2019**, *206*, 315–326. [[CrossRef](#)]
36. Villaverde, M.; Bertero, N.; Garetto, T.; Marchi, A.J. Selective liquid-phase hydrogenation of furfural to furfuryl alcohol over Cu-based catalysts. *Catal. Today* **2013**, *213*, 87–92. [[CrossRef](#)]
37. Marchi, A.; Fierro, J.; Santamaría, J.; Monzón, A. Dehydrogenation of isopropyl alcohol on a Cu/SiO₂ catalyst: A study of the activity evolution and reactivation of the catalyst. *Appl. Catal. A Gen* **1996**, *142*, 375–386. [[CrossRef](#)]
38. Van Der Grift, C.; Mulder, A.; Geus, J. Characterization of silica-supported copper catalysts by means of temperature-programmed reduction. *Appl. Catal.* **1990**, *60*, 181–192. [[CrossRef](#)]
39. Li, H.; Ban, L.; Wang, Z.; Meng, P.; Zhang, Y.; Wu, R.; Zhao, Y. Regulation of Cu Species in CuO/SiO₂ and Its Structural Evolution in Ethynylation Reaction. *Nanomaterials* **2019**, *9*, 842. [[CrossRef](#)] [[PubMed](#)]
40. Bridier, B.; Lopez, N.; Pérez-Ramírez, J. Partial hydrogenation of propyne over copper-based catalysts and comparison with nickel-based analogues. *J. Catal.* **2010**, *269*, 80–92. [[CrossRef](#)]
41. Shao, Y.; Sun, K.; Li, Q.; Liu, Q.; Zhang, S.; Liu, Q.; Hu, G.; Hu, X. Copper-based catalysts with tunable acidic and basic sites for the selective conversion of levulinic acid/ester to γ -valerolactone or 1,4-pentanediol. *Green Chem.* **2019**, *21*, 4499–4511. [[CrossRef](#)]
42. Zaki, M.I.; Hasan, M.A.; Al-Sagheer, F.A.; Pasupulety, L. In situ FTIR spectra of pyridine adsorbed on SiO₂-Al₂O₃, TiO₂, ZrO₂ and CeO₂: General considerations for the identification of acid sites on surfaces of finely divided metal oxides. *Colloids Surf. A Physicochem. Eng. Asp.* **2001**, *190*, 261–274. [[CrossRef](#)]
43. Penkova, A.; Bobadilla, L.F.; Romero-Sarria, F.; Centeno, M.A.; Odriozola, J.A. Pyridine adsorption on NiSn/MgO-Al₂O₃: An FTIR spectroscopic study of surface acidity. *Appl. Surf. Sci.* **2014**, *317*, 241–251. [[CrossRef](#)]
44. Mondal, P.; Sinha, A.; Salam, N.; Singha Roy, A.; Nikhil Jana, R.; Islam, S.M. Enhanced catalytic performance by copper nanoparticle-graphene based composite. *RSC Adv.* **2013**, *3*, 5615–5623. [[CrossRef](#)]
45. Mordekovitz, Y.; Shoval, Y.; Froumin, N.; Shmuel, H. Effect of Structure and Composition of Non-Stoichiometry Magnesium Aluminate Spinell on Water Adsorption. *Materials* **2020**, *13*, 3195. [[CrossRef](#)]
46. Czernohorsky, M.; Seidel, K.; Kühnel, K.; Niess, J.; Sacher, N.; Kegel, W.; Lerch, W. High-K metal gate stacks with ultra-thin interfacial layers formed by low temperature microwave-based plasma oxidation. *Microelectron. Eng.* **2017**, *178*, 262–265. [[CrossRef](#)]
47. Gupta, D.; Saha, B. Dual acidic titania carbocatalyst for cascade reaction of sugar to etherified fuel additives. *Catal. Commun.* **2018**, *110*, 46–50. [[CrossRef](#)]
48. Long, J.; Zhao, W.; Xu, Y.; Li, H.; Yang, S. Carbonate-Catalyzed Room-Temperature Selective Reduction of Biomass-Derived 5-Hydroxymethylfurfural into 2,5-Bis(hydroxymethyl)furan. *Catalysts* **2018**, *8*, 633. [[CrossRef](#)]
49. Robinson, J.W. *Practical Handbook of Spectroscopy*, 1st ed.; CRC Press, Taylor and Francis Group: Boca Raton, FL, USA, 1991.
50. Han, J.; Kim, Y.; Jang, H.; Hwang, S.; Jegal, J.; Kim, J.; Lee, Y. Heterogeneous zirconia-supported ruthenium catalyst for highly selective hydrogenation of 5-hydroxymethyl-2-furaldehyde to 2,5-bis(hydroxymethyl)furan in various *n*-alcohol solvents. *RSC Adv.* **2016**, *96*, 93394–93397. [[CrossRef](#)]
51. Marchi, A.; Gordo, D.; Trasarti, A.; Apesteguía, C. Liquid phase hydrogenation of cinnamaldehyde on Cu-based catalysts. *Appl. Catal. A Gen.* **2003**, *249*, 53–67. [[CrossRef](#)]
52. He, Y.; Fan, J.; Feng, J.; Luo, C.; Yang, P.; Li, D. Pd nanoparticles on hydrotalcite as an efficient catalyst for partial hydrogenation of acetylene: Effect of support acidic and basic properties. *J. Catal.* **2015**, *331*, 118–127. [[CrossRef](#)]
53. Hu, S.; Xue, M.; Chen, H.; Shen, J. The effect of surface acidic and basic properties on the hydrogenation of aromatic rings over the supported nickel catalysts. *Chem. Eng. J.* **2010**, *162*, 371–379. [[CrossRef](#)]
54. Villaverde, M.; Garetto, T.; Marchi, A.J. Liquid-phase transfer hydrogenation of furfural to furfuryl alcohol on Cu-Mg-Al catalysts. *Catal. Commun.* **2015**, *58*, 6–10. [[CrossRef](#)]
55. Dandekar, A.; Vannice, M.A. Determination of the Dispersion and Surface Oxidation States of Supported Cu Catalysts. *J. Catal.* **1998**, *178*, 621–639. [[CrossRef](#)]